hardware

MDPI

Article

CO_2-SASS: A Modular Test Rig for the Scientific Assessment of Heat Transfer of Carbon Dioxide in the Supercritical State

Camila Pedano-Medina [1,2,3,*], Paolo Petagna [1] and Susanne Gleissle [2]

[1] European Organization of Nuclear Research, 1211 Geneva, Switzerland
[2] Faculty of Mechanical and Process Engineering, Offenburg University of Applied Sciences, 77652 Offenburg, Germany
[3] Institute of Thermal Process Engineering, Karlsruhe Institute of Technology, 76131 Karlsruhe, Germany
* Correspondence: camila.pedano@cern.ch

Abstract

Supercritical carbon dioxide (sCO_2) is characterized by low viscosity and a peak in specific heat capacity near the pseudo-critical point, making it a promising coolant for microelectronics. However, most existing sCO_2 test rigs are designed for large-scale thermodynamic cycle studies and lack the capability for controlled, localized heat transfer measurements in small channels. This work presents CO_2-SASS (Scientific Assessment of heat transfer in the Supercritical State), a modular, high-pressure test rig designed to measure local heat transfer coefficients and pressure drops in stainless-steel tubes with diameters on the order of 1-3 mm. The system provides independent control of pressure, mass flow and heating, with direct local wall and fluid temperature as well as precise absolute and differential pressure measurements. Particular emphasis is placed on high-accuracy temperature acquisition, including individual thermocouple calibration and cold-junction bias correction. A detailed uncertainty analysis highlights the dominant role of temperature measurement accuracy, especially for small wall–fluid temperature differences near the pseudo-critical point.

Keywords: carbon dioxide; cooling; supercritical; microelectronics; heat transfer coefficient; pressure drop; experimental; small channel

1. Introduction

In the field of thermal management, supercritical carbon dioxide (sCO_2) has gained significant attention as a promising coolant for various applications, particularly in high-performance heat exchangers and microelectronics cooling. The favorable thermophysical properties of sCO_2—such as its high density, low viscosity and large specific heat capacity near the critical point—enable the development of compact heat exchangers, significantly reducing the size of thermal systems while maintaining performance [1]. This compactness and thermal efficiency make sCO_2 particularly applicable in microelectronics cooling, where space constraints and high heat fluxes are common. A preliminary study by ElGenk demonstrated its viability in such applications [2], where high heat transfer coefficients were reported in an additively manufactured cold plate. Furthermore, Fronk and Rattner [3] discussed the potential use of sCO_2 as the working fluid for high-flux thermal management. They highlighted the need for key research before its practical application, including solving the uncertainty in supercritical heat transfer coefficients and characterizing the heat transfer effects in small channels.

As most of the research on supercritical fluids throughout history has been focused on nuclear reactor cooling applications, studies so far have had very different conditions

Check for updates

Received: 2 October 2025
Revised: 2 March 2026
Accepted: 16 March 2026
Published: 1 April 2026

Copyright: © 2026 by the authors. Licensee MDPI, Basel, Switzerland. This article is an open access article distributed under the terms and conditions of the Creative Commons Attribution (CC BY) license.

compared to those typical in microelectronics cooling, the most important one being the pipe diameter. For CO_2, most studies have measured heat transfer coefficients in heated pipes with sizes ranging 4 to 10 mm, see [4–6]. Only two studies have reported convective heat transfer coefficients in pipe sizes below 2 mm [7,8] and they have not provided enough conclusive data to properly understand the effect of different system variables: inlet temperature, hydraulic diameter, and heat flux. Additionally, they only reported heat transfer coefficients and failed to comment on the pressure drop results, although their test rigs did measure them.

The potential of supercritical CO_2 as a coolant arises from the change in its thermophysical properties around the critical region. Figure 1 shows the variation in density, heat capacity, viscosity, and thermal conductivity with temperature at different pressures. The critical point of CO_2 is at 73.8 bar. Below this value, at subcritical conditions, an isobaric addition of heat into a system induces boiling and therefore the coexistence of liquid and vapor phases. Above it, two distinct phases can no longer coexist and the fluid instead behaves as a single phase with properties that combine features of both liquids and gases: a liquid-like density, which enhances convective heat transfer per unit volume, and a gas-like viscosity, which reduces pumping power requirements.

A particularly interesting feature occurs near the so-called pseudo-critical point (The pseudo-critical point refers to a physical condition, in pressure and temperature, at which the heat capacity of a fluid above the critical point experiences a maxima), where the specific heat capacity exhibits a pronounced peak. In this regime, large amounts of heat can be absorbed with only a modest increase in fluid temperature. However, this sharp dependence on pressure and temperature also explains why cooling with supercritical fluids remains difficult to characterize. Small variations in operating conditions strongly affect the heat transfer response, and existing correlations often fail to reproduce experimental data consistently. Up to date, no universally applicable correlation for a given geometry has been established [9], highlighting the need for systematic parametric measurements.

This lack of consistent correlations is closely linked to the extreme sensitivity of heat transfer coefficients near the pseudo-critical region. Even minor deviations in measured temperature or pressure can cause large variations in the calculated values. As a result, reported data in the literature often differ significantly from one another [10].

Moreover, the experimental tools available to explore the potential of sCO_2 as a refrigerant remain limited. Most existing test rigs are developed for applications such as thermodynamic cycle optimization, turbomachinery validation, or compact heat exchanger design, often focusing on integral system performance rather than localized thermal behavior. These setups typically operate at high total flow rates in larger channels, and are not designed to study the localized heat transfer behavior at the high mass fluxes and small hydraulic diameters relevant to microelectronics-scale applications. As a result, they lack the flexibility to conduct controlled, repeatable parametric studies of sCO_2 heat transfer under conditions relevant to small-scale, high-flux thermal management.

To address this gap, a modular test rig has been designed and constructed in order to investigate sCO_2 heat transfer across a wide range of flow rates, pressures, and heat fluxes under conditions relevant to microelectronics cooling. The system enables direct measurement of local wall and fluid temperatures, as well as pressure drop across a small-diameter test section (in the range of 1 to 3 mm), additionally offering the flexibility to adjust layout, inlet conditions and sensor positioning for high-resolution thermal characterization.

Finally, the operating conditions of the test rig have been selected to enable direct comparison between subcritical and supercritical regimes. By using the same instrumentation and equipment, the setup can replicate both evaporative heat transfer below the critical point and single-phase heat transfer above it. This unique capability allows systematic

investigation of the fundamental differences between the two regimes, which remain poorly understood and insufficiently documented in the literature [5].

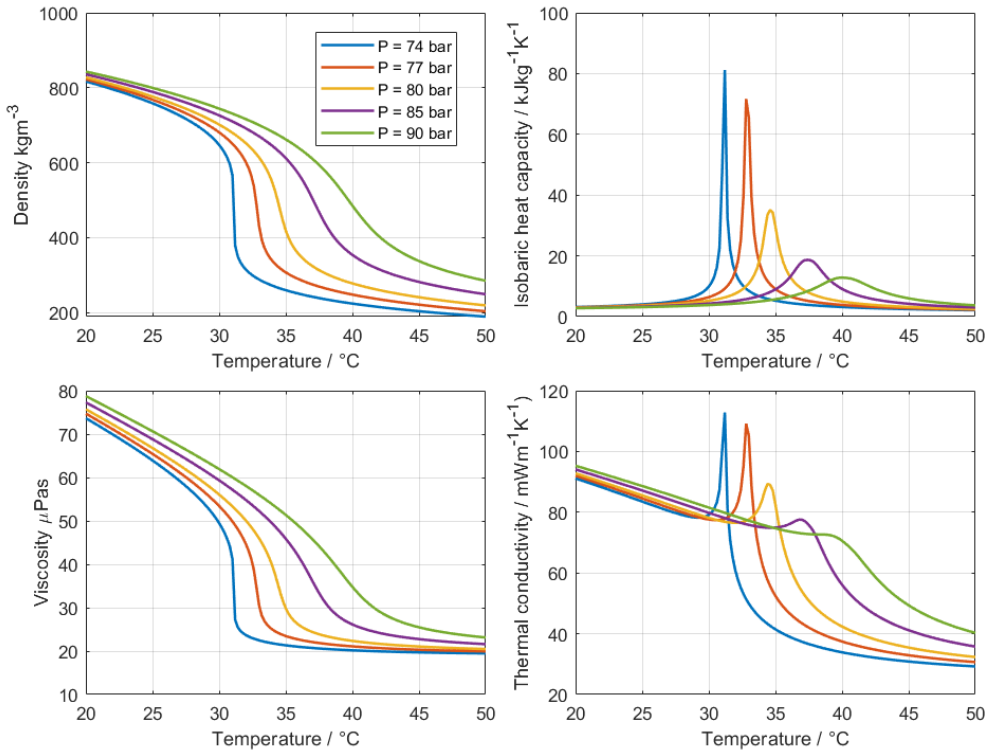

Figure 1. Thermophysical properties of CO_2 as a function of temperature (20 to 50 °C) at selected pressures (70, 75, 80, 85, 90 bar). Shown are: density (kg m^{-3}), heat capacity at constant pressure (c_p, kJ kg^{-1} K^{-1}), viscosity (μ, µPa s), and thermal conductivity (k, mW m^{-1} K^{-1}). Property values were obtained from REFPROP [11].

2. Design

The test rig was designed to investigate sCO_2 heat transfer in a capillary geometry, with precise control over pressure, mass flow rate, heat input, and flow orientation. The process and instrumentation diagram (P&ID) is shown in Figure 2. A detailed description is included in this section, as well as the Bill of Materials (Table 1). As this section contains all the necessary information respective to hardware, Table 2 lists the sensor uncertainties, while their specific calculation methods are detailed further in Section 6. Operating instructions are included in Section 4.

Carbon dioxide is pressurized by using nitrogen gas inside a combined metal bellows–piston accumulator (AC101), equipped with a cooling coil. The bellows and piston sections are mechanically coupled, enabling a maximum displacement volume of 3 L. This configuration allows for dynamic pressure regulation while fully isolating the nitrogen and CO_2 sides, preventing any cross-contamination.

The accumulator serves as the system's pressure setpoint controller and maintains pressures in the 50–120 bar range. It also functions as a thermal buffer, stabilizing the stored liquid by accommodating volume changes and avoiding pressure spikes. Although the role of the accumulator is functionally similar to that of a commercial hydraulic accumulator, a custom design was implemented to ensure the long-term safety and purity of the working fluid. Several alternatives were considered, including piston, bladder/diaphragm, and bellows accumulators. However, while piston and bladder types could allow long-term nitrogen permeation, metal bellows are highly sensitive to overpressure. In this regard, given the long-term nature of the experimental program and the involvement of multiple

operators, a fail-safe configuration was prioritized. This led to the selection of a coupled piston–bellows accumulator, which combines the contamination-free characteristics of bellows with the mechanical robustness of a piston. While the exact internal configuration of the current accumulator is proprietary, equivalent functionality could be achieved using a coupled system of two commercially available accumulators: one charged with a high-pressure gas and one containing CO_2, mechanically linked to transmit pressure without fluid contact.

Alternatively, if maintaining strict fluid purity is essential, for example, in experiments targeting precise heat transfer coefficient measurements, a single metal bellows accumulator can be used, provided it is paired with a carefully designed control strategy to manage system filling and pressure adjustments. On the other hand, for less demanding applications, where a small degree of nitrogen–CO_2 cross-contamination is acceptable, a piston accumulator with a PTFE seal may offer a simpler and more cost-effective solution.

Downstream of the accumulator, the fluid is circulated by a magnetically driven rotary vane pump (LP101), controlled by a variable-frequency drive (VFD). As this is a dry pump, the continuously rotating cartridge (housing the vanes) is subject to wear. This means that clearances gradually increase and the pump is expected to lose head and therefore flow performance over time. Absolute pressure is measured before and after the pump to monitor this degradation. An inline filter (FL101) removes debris immediately downstream. To allow for continuous operation without emptying the test rig, two filters in parallel are installed. With time, the filter will become saturated with debris and have to be cleaned. An absolute pressure sensor has been installed directly downstream to detect increasing pressure drops and switch between filters. To protect the pump and maintain stable operation, a bypass valve (MV101) is installed directly downstream. This ensures continuous circulation even when flow demand is low, avoiding conditions where the pump would otherwise operate at insufficient flow rates.

The remaining mass flow rate is measured by a Coriolis flow meter (FT101), which measures the actual flow passing through the test section. In this section of the rig, two manual valves (MV106 and MV107) can be used to characterize and diagnose the pump. During normal operation, the regulation valve is kept fully open and the three-way valve always points at the test section. The fluid is then preheated using an electric heater (EH101) before entering the test section. Temperatures are measured up- and downstream of the electric heater to monitor its correct operation.

After this, the fluid enters the test section, which consists of a 1 m long stainless-steel (304L) capillary with an inner diameter of 1.00 mm and outer diameter of 1.59 mm. Resistive heating is applied via clamped electrodes (EH102), powered by a DC power supply. To avoid parasitic current leakage, dielectric fittings are placed at both ends of the test section. Up- and downstream adiabatic segments ensure flow development prior to the heated zone.

Wall temperatures are measured at eleven points along the heated pipe using K-type thermocouples directly attached to the outer surface. The sensors are calibrated as described in Section 5.2 and installed afterwards using epoxy steel putty and thermal paste. In-fluid PT-100 temperature sensors are also installed at both the inlet and outlet of the test section, while absolute pressure is measured only at the inlet. Instead of direct pressure measurement at the outlet, a differential pressure sensor measures pressure drop along the tested area. After the test section, the fluid passes through a compact heat exchanger, cooled by a chiller unit (CU101), before returning to AC101 to complete the loop.

The entire test section is mounted within an insulated, tiltable support frame, enabling experiments at various flow orientations without modifying instrumentation. The test section can also be easily removed, so that different types of pipes or configurations can be tested using the same rig (see Figure 3).

Table 1. Bill of Materials (BOM) for CO_2-SASS.

Quantity	Component	Source/Manufacturer	Material Type	Approx. Cost/Unit (EUR)
1	Piston–bellows accumulator (AC101)	HYDAC (bespoke design)	Stainless steel	Upon request
3	High-purity bursting disc (BD101)	Schlesinger, Type U	Stainless steel	500
1	Chiller unit (CU101)	Van der Heijden, VDH5000A	Mixed metals/plastics	15,000
1	Electric heater (EH101)	WATLOW, CAST X-500	Stainless steel/aluminium	1500
2	Inline filter (FL101)	LEWA, FMI2, 3 µm	Stainless steel	600
1	Pressure regulator (FR101)	Gloor, 200 bar	Stainless steel	500
1	Plate heat exchanger (HX101)	SWEP, B4THx30	Stainless steel	160
1	Rotary vane pump (LP101)	M-PUMPS, VA01 MODULAR 2S	Stainless steel	19,000
1	High-pressure relief valve (RV101)	Parker, HPRV	Stainless steel	600
10	Manual valves (MV, shut-off)	Swagelok, 43 G Series	Stainless steel	160
3	Manual valves (MV, regulation)	Swagelok, 31 Series	Stainless steel	150
10	PT100 in-fluid temperature sensors	Rodax, Class A, 4-wire	Platinum RTD	120
11	K-type wall thermocouples	Roessel Messtechnik	NiCr/NiAl	14
7	Absolute pressure sensors (PT1xx)	Keller AG, 23SX	Stainless steel	380
1	Differential pressure transmitter	Endress+Hauser, PMD75B	Stainless steel	2800
1	Thermal insulation sheet	RS Components	Glass wool	120
1	Thermal insulation	Armacell, Armaflex	Elastomer foam	Upon request
-	Fittings	Swagelok	Stainless steel	Upon request
-	Structural aluminium extruded profiles	Aldiance	Aluminium	Upon request

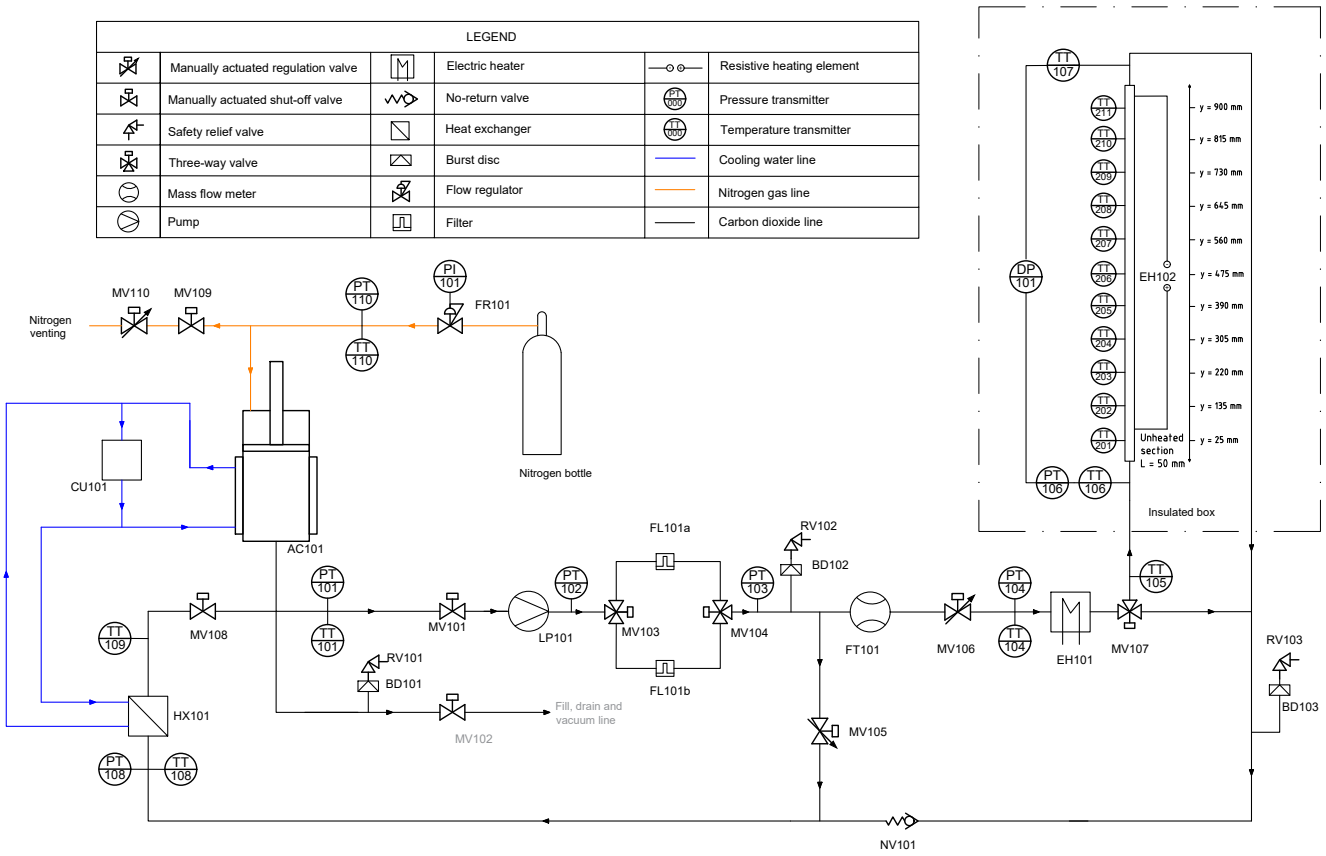

Figure 2. Piping and instrumentation diagram (P&ID) of the CO_2-SASS setup. All major components are shown, including pressure and temperature sensors (PT, TT respectively), heaters, valves, and flow elements.

Table 2. System variable sensors: nomenclature, type of sensor and their uncertainties.

Measured Variable	Designator	Number	Sensor Type	Derived Uncertainty
Absolute pressure	PT	101–110	Piezoresistive sensor	0.2 bar
Differential pressure	DP	201	Capacitive sensor	0.003 bar
Mass flow	FT	101	Coriolis flow meter	0.04 g/s
Fluid temperature	TT	101–110	PT100	0.05 K (after calibration)
Wall temperature	TT	201–211	Type K thermocouple	0.07 K (after calibration)

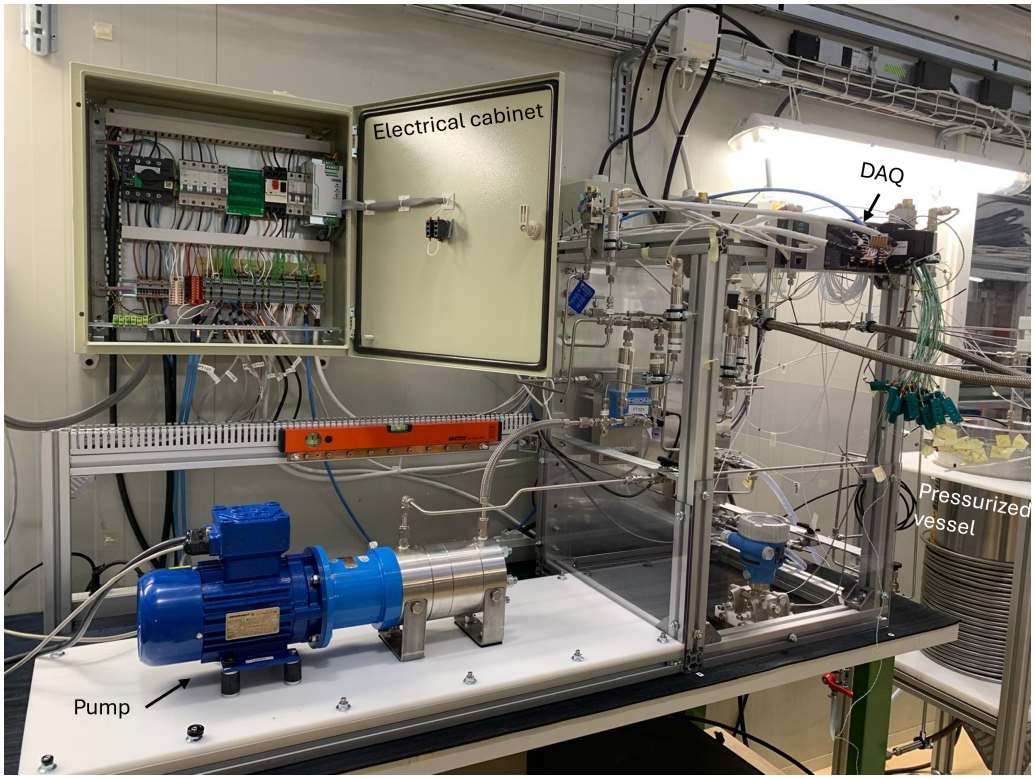

(**a**)

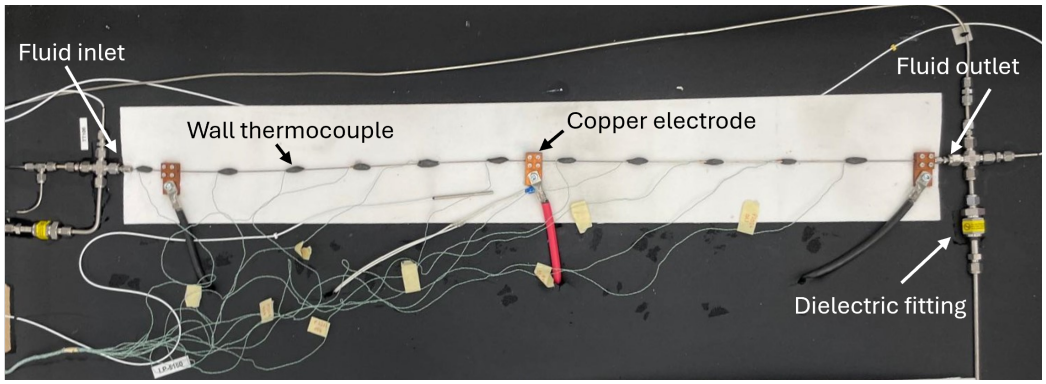

(**b**)

Figure 3. Images of the CO_2-SASS experimental system. (**a**) Full view of the assembled rig, including electrical cabinet (left), rotary vane pump (front, blue) and piping. (**b**) Heated test section equipped with eleven wall thermocouples, copper electrodes for resistive heating, inlet/outlet PT100 probes, and dielectric fittings for electrical insulation.

Data acquisition and control are handled using National Instruments (NI) hardware and custom LabVIEW-based software (version 24) for process control and logging. Process signals and parameters are collected in a cDAQ-9178, which forms the heart of the monitoring system. Figure 4 summarizes the modules and their associated signal types. While a detailed explanation of each module is omitted here for brevity, except for the uncertainty derivation discussed in Section 5.2, interested readers may refer to the figure and manufacturer website for further insight.

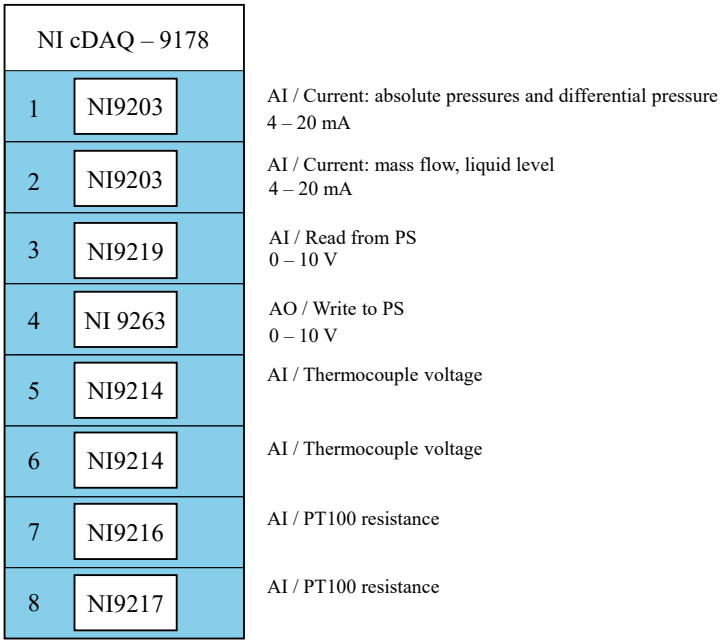

Figure 4. Schematic representation of the NI modules in the test rig and their corresponding signal types.

3. Build Instructions

The construction of the CO_2-SASS rig follows directly from the design choices described in Section 2. The steps below outline the assembly process in sufficient detail to enable reproduction.

1. Frame and structural support: Assemble the main support frame using extruded aluminium profiles. The frame must be dimensioned to accommodate the accumulator, pump, filters, heat exchanger, and test section. Install an insulated tiltable mount for the test section to allow experiments at different orientations, if desired.
2. Piping: Use stainless-steel 316 L tubing with a 4 mm inner diameter and a 6 mm outer diameter for the main CO_2 loop. For the pressure sensor lines, use 1/8 in. OD stainless-steel tubing. Connect all tubing with Swagelok VCR fittings to facilitate repeated assembly and disassembly without loss of sealing performance.
3. Accumulator (AC101): Install the piston–bellows accumulator upstream of the pump. Connect one side to the CO_2 loop and the other to the nitrogen regulator (FR101) for pressure control. Ensure a cooling coil is fitted around the accumulator body for thermal stabilization.
4. Pump and filters: Mount the magnetically driven rotary vane pump (LP101) downstream of the accumulator. Install a bypass valve (MV105) directly after the pump outlet to protect against low-flow conditions. Place two inline filters (FL101) in parallel, with valves to isolate each filter for maintenance. Connect an absolute pressure sensor downstream of the filters to monitor clogging.

5. Flow and heating section: Install the Coriolis flow meter (FT101) downstream of the filters. Place the electric preheater (EH101) after the flow meter. Install manual MV106 and MV107 valves to allow pump characterization during commissioning.
6. Test section: Mount the 1 m stainless-steel capillary (1.00 mm ID, 1.59 mm OD) within the insulated tiltable support. Attach copper electrodes for resistive heating (EH102) at both ends, ensuring dielectric fittings prevent leakage currents. Apply thermal paste and epoxy steel putty to fix eleven K-type thermocouples (TT201–TT211) along the outer wall. Install PT100 probes at the inlet and outlet, and connect the differential pressure transmitter to the test section ends.
7. Cooling section: Route the outlet flow through the plate heat exchanger (HX101), cooled by the chiller unit (CU101). Connect the return line to the accumulator to close the loop.
8. Instrumentation and control: Connect all pressure, temperature, and flow sensors to the NI cDAQ-9178 chassis, using the modules specified in Figure 4. Wire the heaters and pump drive to the control cabinet. Install safety devices, including the high-pressure relief valve (RV101) and bursting discs (BD101), at appropriate positions.
9. Insulation: Apply glass wool insulation sheets around the test section and thermally insulating elastomer foam around the tubing to minimize heat loss and ensure stable thermal conditions.

All parts listed in Table 1 are commercially available and can be assembled using standard laboratory tools. Deviations such as larger tubing diameters or alternative valves may be implemented depending on the target flow rate and available equipment.

4. Operating Instructions

4.1. Filling the System

The system must be fully vacuumed before charging it with carbon dioxide. A vacuum pump is connected to MV102 and left for one hour, with all the rest of the valves open to properly vent the entirety of the setup of any air. Afterwards, a bottle containing two-phase carbon dioxide (quality 48), equipped with a pressure regulator, is placed on a scale and connected to the same valve. The line is then filled with liquid carbon dioxide while keeping MV102 in a closed position. This step ensures that there is no air going inside the setup from the hose. The scale is then zeroed.

MV102 is then opened again to allow carbon dioxide to flow inside the system. Once stabilized, the regulator is further opened to increase the pressure on the system side. The pressure is firstly set to 20 bar and allowed to equalize for 15 min. Then, the pressure is increased in 10-bar increments and allowed to rest. Finally, when the pressure of the bottle has been reached, the system is allowed to stabilize. MV102 is closed when the scale measurement has reached 2.5 kg.

The fill pressure will be the maximum pressure attainable with the CO_2 bottle, which will depend on the mass contained and the ambient temperature. To achieve higher pressures inside the rig, nitrogen has to be filled on the other side of the accumulator. For this, FR101 must be opened to pressurize with nitrogen gas. A very precise control of the system pressure can be achieved when working together with FR101, to allow nitrogen in the system, and MV110, to vent excess pressure.

4.2. Steady Operation

To operate the test rig, firstly an initial operating pressure is chosen and set with FR101. The pump LP101 can then be started to set a stable operating condition. After equalization of temperatures, depending on the initial state, the pressure will have changed and can be readjusted to its desired value in PT106 by means of opening MV110. The mass flow can

also be adjusted to the value of interest using MV105. Heaters EH101 and/or EH102 will then be used depending on the nature of the tests to be carried out. This is done by means of LabVIEW software, which can be found in the Supplementary Materials.

A steady-state point is considered only when the temperature variation at each sensor remains within ± 0.05 K for a period of five minutes, ensuring negligible transient effects. This threshold is well below the absolute uncertainty of the temperature sensors and confirms thermal stability during each measurement point. At the moment, due to the nature of the software, the acquisition rate is fixed at 1 Hz; however, it is planned to remove this constraint in the future.

5. Fundamentals

5.1. Convective Heat Transfer Coefficient

In convective heat transfer, the local heat transfer coefficient represents the rate of heat transfer per unit area and per-unit temperature difference between the surface and the fluid. This coefficient is the most fundamental parameter of convective heat transfer, while at the same time its derivation is highly indirect: the value is obtained after a long chain of measurements and is therefore heavily affected by errors. The SI units are W/m^2K and its value can be experimentally derived as:

$$\alpha = \frac{q''}{T_{w,i} - T_b}, \tag{1}$$

where q'' is the local heat flux, obtained from the heat flow (Q) per unit area:

$$q'' = \frac{Q}{A}, \tag{2}$$

calculated by evaluating the enthalpy rise of the working fluid across the test section.

$$Q = \dot{m} \cdot (h_{\text{out}} - h_{\text{in}}) \tag{3}$$

Here, $\dot{m}$ is the measured mass flow rate, and h_{in}, h_{out} are the specific enthalpies at the inlet and outlet of the heated section, respectively. Inlet enthalpy is calculated using directly measured pressure and temperature values, while outlet enthalpy is obtained from the outlet temperature and the pressure value is determined as $P_{\text{out}} = P_{\text{in}} - \Delta P$, with ΔP measured across the entire test section (DP101 in Figure 2).

5.2. General Uncertainty Calculation

The derived uncertainties for all measured variables are obtained using the standard uncertainty propagation method based on a first-order Taylor series expansion:

$$u_y = \sqrt{\sum_{i=1}^{n} \left(\frac{\partial y}{\partial x_i} \cdot u_{x_i} \right)^2} \tag{4}$$

In this formula, u_y is the overall uncertainty of the result variable y, which is affected by the uncertainties u_{x_i} of the other variables x_i it depends on. The terms $\frac{\partial y}{\partial x_i}$ are called sensitivity coefficients and show how much the result changes when each variable x_i changes.

This approach assumes that the input variables are uncorrelated. In cases where strong correlations are present, a full covariance matrix is required. All reported uncertainties correspond to one standard deviation (1σ), unless otherwise noted.

In practical terms, when the measured variables are not strongly dependent on one another, the total uncertainty is simply the square root of the sum of the squares of the individual uncertainties.

6. System Calibration and Measurement Uncertainty

Wall temperatures are universally measured using thermocouples when the pipe size is below 2 mm in supercritical systems (Whenever space allows, RTDs would be preferred for simpler and more accurate temperature measurements. NTCs could also be an option, although unfortunately are not yet commonly used in the field). However, the methods for their placement and signal interpretation vary significantly across studies, as there is no established standard. In some cases, thermocouples are sheathed and embedded in a copper block surrounding the heated section [8]. In other cases, thermocouples are directly soldered or spot-welded to the pipe wall [4], which reduces thermal mass and contact resistances but is not feasible in thin-walled tubes.

Moreover, a key element that is rarely addressed in detail when using thermocouples is the treatment of the cold junction. While modern acquisition systems offer automatic cold junction compensation, the typical accuracy of these modules (cold junction temperature measurement accuracy) is on the order of ± 0.25 K to ± 1 K. Any errors in reading the cold junction temperature will contribute directly to errors in the final temperature measurement if one considers Taylor's propagation of uncertainty. Some studies report thermocouple uncertainties below this limit, without clarifying the reference method or compensation strategy used. Whether this is due to post-calibration, unreported ice bath references, or optimistic estimates remains unclear. The lack of transparent discussion on this topic further complicates the comparison of heat transfer data across the literature and could be one of the main contributors to the scattered distribution of the data at supercritical conditions.

All temperature measurements in CO_2-SASS have been referenced to the ITS-90 temperature scale.

6.1. Thermocouples

Type K thermocouples were used for wall temperature measurements. To characterize each individual thermocouple in the DAQ chain, they were embedded in an in-house built copper block, submerged in a temperature-controlled bath. An insert was machined to tightly contain the probes, which were covered in electrical insulation beforehand and placed inside the insert, together with thermal paste. Figure 5 shows the different steps and equipment used for the calibration. A range of temperatures from 0 to 100 °C was covered, in intervals of 10 °C. The voltage measured by each thermocouple was compared to that of a Fluke SPRT (Standard Platinum Resistance Thermometer) embedded in the same copper block, at a similar height. Voltage signals were acquired using NI-9214 modules. The uncertainty of the temperature signal in this case includes sensor tolerance, thermoelectric voltage nonlinearity, and cold junction error.

To correct systematic measurement bias, a calibration equation was obtained for each thermocouple. The problem of thermocouples is that one can get as precise as the cold junction can get, and this can really spoil the whole process of calibration. To counter this, the cold junction was calibrated with a probe placed in an ice bath at the same time as the rest of the sensors. The ice bath was achieved by filling a container with crushed ice and covering the volume with water, as specified by the National Institute of Standards and Technology [12]. The mixture was then mixed and left to sit inside a polystyrene box for some seconds right before starting the recording via the software for data acquisition. This was only performed when the temperature of the probes inside the copper block was considered stable.

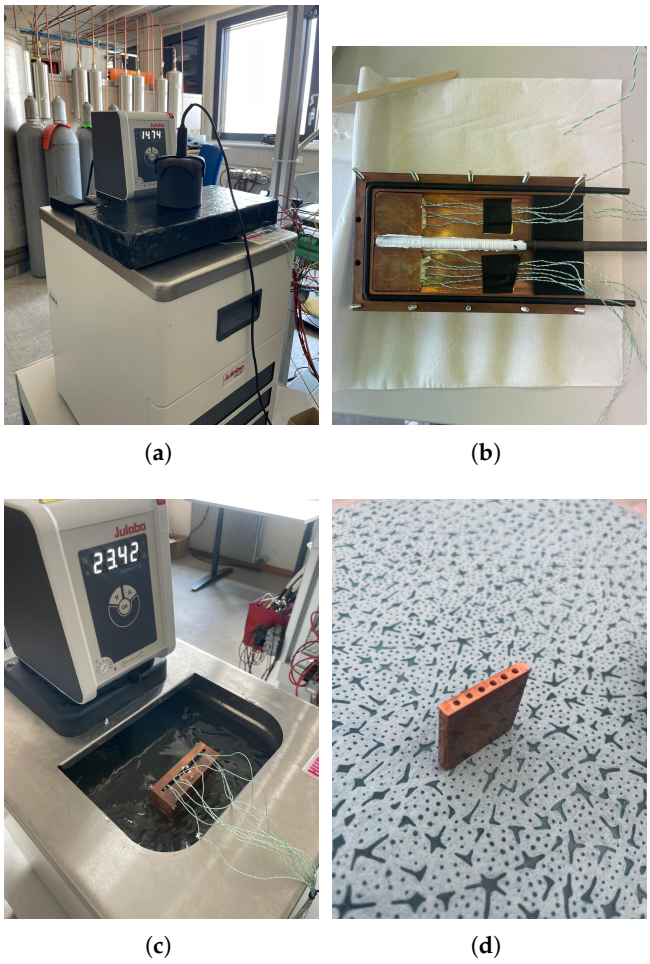

Figure 5. Steps and equipment used for the calibration of thermocouples. (**a**) Chiller unit used in the calibration setup; (**b**) copper block used to hold sensors; (**c**) copper block submerged in temperature-controlled bath; (**d**) small copper insert for thermocouple positioning.

This correction ensures consistency with the ice bath calibration and improves measurement accuracy by compensating for the cold junction bias. However, having an ice bath constantly ready and available during an entire data campaign could be quite impractical. For the first results of the rig, a method was followed so that the ice bath was prepared once per day. This procedure assumes that the cold junction temperature remained stable during the testing time, which is valid considering that the temperature in the laboratory did not change significantly from the morning to the afternoon.

In practice, the calibration using the electronic cold junction will be used for all thermocouple measurements, due to its practicality during continuous operation. The ice bath is instead prepared once per day to evaluate the cold junction bias, which is then treated as a constant voltage correction (typically ≈ 0.01 mV) applied to all measurements of that day. Therefore, the ice bath is not used to generate a separate calibration curve, but to correct the electronic CJC-based calibration for systematic error once per day.

The rest of the components of the wall temperature measurement were the uncertainty of the polynomial conversion (0.05 K), the voltage measurement uncertainty of the DAQ module (0.035 K) and the uncertainty of the SPRT (0.01 K) and its readout (0.006 K). These, combined with the regression uncertainty and inserted into Equation (4), result in an uncertainty of 0.066 K.

The calibration procedure is included in Appendix A.

6.2. PT100

PT100 resistance temperature detectors (RTDs) are used to measure fluid temperatures. The resistance is acquired using NI 9216 and 9217 modules. The uncertainty was derived considering the calibration error and DAQ module resolution.

The calibration curve of each sensor was obtained following the ITS-90 standard [13] for PT100. The calibration process was carried out in a controlled temperature bath set to a series of fixed setpoints spanning the range from 0 °C to 100°C. Additionally, measurements at the triple point of water (TPW) were included to provide an absolute reference.

For each setpoint, sensor resistances and the Fluke SPRT reference temperature were recorded simultaneously using a LabVIEW script.

The procedure for the application of the ITS-90 is included in Appendix B.

The total resultant error of the PT100 calibration is 0.006 K. Combining this with the DAQ card error (0.05 K) and the SPRT and readout error, with the same values used for the thermocouples, results in a total maximum error of 0.05 K for the fluid temperature.

6.3. Pressures

Absolute and differential pressures were measured using piezoresistive and capacitive sensors. The accuracy of the absolute pressure measurement is a function of the measured value, and it is reported by the manufacturer as 0.1%. Considering that the measurement range for the sensors on the CO_2 side is 0–160 bar, the maximum absolute error is 0.16 bar. For the nitrogen side, the sensor has a higher range, up to 200 bar, resulting in an absolute error of 0.2 bar.

The differential pressure sensor has an accuracy of 0.075%. As the maximum value is 3 bar, this results in a 0.002 bar absolute error.

The error of the acquisition card NI9203 is given by the manufacturer and is 0.0132 mA. Combining this with the individual sensor sensitivities and adding it to the sensor error calculation results in:

1. CO_2 absolute sensors: 0.2 bar.
2. N_2 absolute sensors: 0.26 bar.
3. Differential sensor: 0.003 bar.

6.4. Pipe Diameter

The inner diameter was measured in five different samples from the same batch via X-ray tomography. The value used for the uncertainty is the standard deviation of the measurements, 0.0007 mm. The pipe roughness was also measured using a contact profilometer and was 1.15 µm.

6.5. Mass Flow

The error in the measurement with the Coriolis flowmeter was combined with that of the acquisition card NI9203. For flows above 0.5 g/s, the flow meter has an error of 0.1%. At the maximum reading value, this results in 0.014 g/s. Combining the module uncertainty with its own resolution gives a final value of ±0.036 g/s for the maximum absolute error attainable.

6.6. Heat Flux

A calorimetric calculation of the heat input by means of a heat balance is performed for data reduction, as will be explained in the coming sections. This procedure ensures that the actual heat input is correctly used. Equation (3) shows the energy conservation equation solved for a horizontal pipe. The uncertainty of the heat flux cannot be extracted

from the voltage and current provided by the power supplies, but is rather a result of other measurements. A detailed procedure of its derivation is shown in Section 8.

7. Data Reduction

The goal of the data reduction is to obtain local wall–fluid temperature differences and heat transfer coefficients along the test section from directly measured signals. The procedure uses a one-dimensional axial discretization of the pipe and evaluates thermophysical properties at each location.

Raw inputs are the inlet/outlet fluid temperatures T_{in} (TT106) and T_{out} (TT107), the inlet absolute pressure P_{in} (PT106), the differential pressure ΔP (DP101) across the test section, the mass flow rate $\dot{m}$, the outer wall thermocouple temperatures at the eleven locations $T_{w,o}(z)$, and the geometric data $(D_i, D_o, L_{\text{heater}}, z_{\text{start}}, z_{\text{end}})$. The cross-section is $CS = \frac{\pi}{4} D_i^2$. The outlet pressure is calculated as:

$$P_{out} = P_{in} - \Delta P \tag{5}$$

The fluid enthalpies at the endpoints are obtained from REFPROP at the measured states,

$$h_{in} = h(T_{in}, P_{in}), \qquad h_{out} = h(T_{out}, P_{out}) \tag{6}$$

and the heat absorbed by the fluid is

$$Q_{\text{fluid}} = \dot{m} \left(h_{\text{out}} - h_{\text{in}} \right) \tag{7}$$

The pipe is divided into 100 N_{seg} axial segments with nodes $z_{seg} \in [0, L]$. The fields $T_p(z)$, $P_p(z)$, and $h_p(z)$ are initialized at the inlet,

$$T_p(0) = T_{\text{in}}, \quad P_p(0) = P_{\text{in}}, \quad h_p(0) = h_{\text{in}}, \tag{8}$$

and updated marching downstream. Over the heated span $[z_{start}, z_{end}]$ the applied heat is distributed uniformly, so that the segment heat and local heat flux are

$$dQ(j) = \frac{Q_{\text{fluid}}}{L_{\text{heater}}} \Delta z, \qquad q''(j) = \frac{dQ(j)}{\pi D_i \, \Delta z} = \frac{Q_{\text{fluid}}}{\pi D_i L_{\text{heater}}}, \tag{9}$$

and $q''(z) = 0$ outside that interval. With ρ, μ, k, C_p evaluated from REFPROP at the current state $(T_p(z), P_p(z))$, the superficial velocity and Reynolds number are

$$v(z) = \frac{\dot{m}}{\rho \, CS}, \qquad Re(z) = \frac{\dot{m} \, D_i}{\mu \, CS} \tag{10}$$

The friction factor is calculated as per Blasius/McAdams depending on the value of the Reynolds number [14,15]:

$$f = \begin{cases} 0.316 \, Re^{-0.25}, & Re < 2 \times 10^4, \\ 0.184 \, Re^{-0.20}, & Re \geq 2 \times 10^4, \end{cases} \tag{11}$$

and the segment pressure drop (Darcy–Weisbach) and enthalpy rise are

$$\Delta P_z = \frac{f \, \rho \, v^2}{2 D_i} \Delta z, \qquad h_p(z+1) = h_p(z) + \frac{dQ(z)}{\dot{m}} \tag{12}$$

The pressure and temperature are recalculated at each segment as:

$$P_p(z+1) = P_p(z) - \Delta P_z, \qquad T_p(z+1) = T\big(h_p(z+1), P_p(z+1)\big), \tag{13}$$

with $T_p(z+1)$ evaluated by REFPROP.

The bulk temperature and pressure at the exact thermocouple axial locations z_{TC} are then obtained by linear interpolation.

The inner-wall temperature is calculated with the one-dimensional solution of the Fourier law for an annular tube with heat generation inside the tube. In this way, the radial temperature drop through the pipe thickness at each thermocouple location is:

$$\Delta T_w = \left(\frac{q\, D_i}{4\lambda_{SS}}\right) CF, \tag{14}$$

where

$$CF = \frac{\psi(1 - ln\psi) - 1}{1 - \psi} \quad \text{and} \quad \psi = \left(\frac{D_o}{D_i}\right)^2 \tag{15}$$

The local inner-wall temperature and the experimental *local* heat transfer coefficient follow directly:

$$\Delta T(z_{TC}) = T_{w,i}(z_{TC}) - T_b(z_{TC}), \qquad \alpha_{exp}(z_{TC}) = \frac{q''_{TC}(z_{TC})}{\Delta T(z_{TC})}. \tag{16}$$

For comparison with a known correlation, the correlation by Gnielinski (Equation (17)) is computed at the same z_{TC} using properties at $T_b(z_{TC})$, $P_b(z_{TC})$ and the friction factor $f(z_{TC})$ interpolated from the segment values. The heat transfer coefficient $\alpha(z_{TC})$ is then calculated with Equation (18), where the thermal conductivity, k, is extracted via REFPROP.

$$Nu_{Gn}(z_{TC}) = \frac{f(z_{TC})}{8} \frac{\big[\mathrm{Re}(z_{TC}) - 1000\big]\ \mathrm{Pr}(z_{TC})}{1 + 12.7\sqrt{f(z_{TC})/8}\,\big(\mathrm{Pr}(z_{TC})^{2/3} - 1\big)} \tag{17}$$

$$\alpha_{Gn}(z_{TC}) = \frac{\mathrm{Nu}_{Gn}(z_{TC})\, k(z_{TC})}{D_i} \tag{18}$$

8. Uncertainty Derivation in CO_2-SASS

Any precise measurement of a heat transfer coefficient should be accompanied by a pressure drop measurement, as well as an accurate estimate of the contributions of all measured uncertainties. Considering Equation (1), the derivation of the uncertainty of the heat transfer coefficient results in:

$$u_\alpha = \sqrt{\left(\frac{\partial \alpha}{\partial q''}\, u_{q''}\right)^2 + \left(\frac{\partial \alpha}{\partial T_w}\, u_{T_w}\right)^2 + \left(\frac{\partial \alpha}{\partial T_b}\, u_{T_b}\right)^2} \tag{19}$$

Considering that

$$\frac{\partial \alpha}{\partial q''} = \frac{1}{T_w - T_b}, \quad \frac{\partial \alpha}{\partial T_w} = -\frac{q''}{(T_w - T_b)^2}, \quad \frac{\partial \alpha}{\partial T_b} = \frac{q''}{(T_w - T_b)^2}; \tag{20}$$

the derived relative uncertainty results in:

$$\frac{u_\alpha}{\alpha} = \sqrt{\left(\frac{u_{q''}}{q''}\right)^2 + \left(\frac{u_{T_w}}{\Delta T}\right)^2 + \left(\frac{u_{T_b}}{\Delta T}\right)^2} \tag{21}$$

In view of Equation (21), the uncertainty of the heat transfer coefficient depends on the individual uncertainties of the heat flux and the temperatures. In general, the higher the heat flux, the higher the temperature difference. At higher heat fluxes, the error in the heat transfer coefficient is lower, while it increases at both small temperature differences and fluxes.

As an example, Figure 6 illustrates the resulting relative error in the heat transfer coefficient as a function of the true temperature difference, assuming a fixed temperature measurement uncertainty of ± 0.2 K and no error in the heat flux measure. In this analysis, the error increases sharply for small ΔT values, reaching over 100% relative error when the temperature difference falls below the uncertainty value. The zoomed figure shows the asymptotic decay of the error at higher temperature differences.

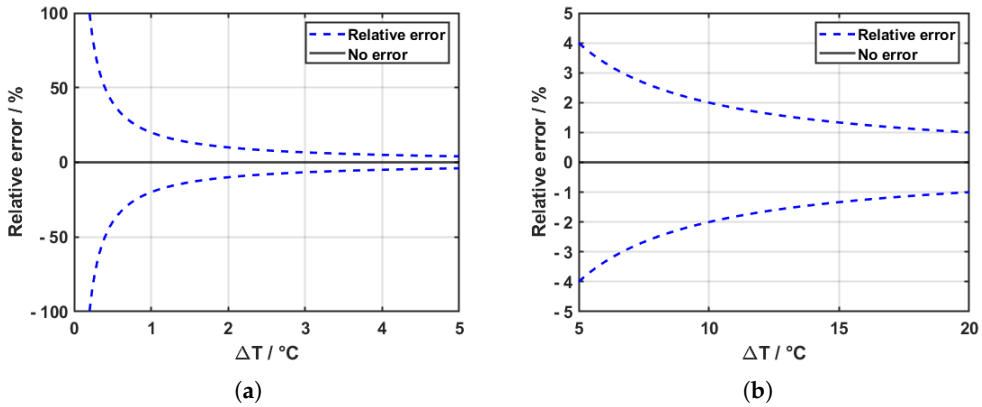

Figure 6. Relative error in the heat transfer coefficient as a function of the true wall–bulk temperature difference ΔT, assuming a fixed measurement uncertainty of ± 0.2 °C. (**a**) Small temperature difference range ($\Delta T < 5$). (**b**) Zoom in for $\Delta T > 5$ °C.

Depending on the method of calculation of the power, the error in the determination of q'' will be related to the voltage and current (see [4]) or to the pressure and temperature. Calculating q'' directly as the product of voltage and current should also be accompanied by an energy balance and a proper calculation of Q_{loss} for every datapoint. This can escalate and result in a complicated task, as the heat loss to ambient will be directly dependent on the heat transfer coefficient of the fluid. For short sections and uniform wall temperatures, this can be simplified. However, for long segments as well as temperature gradients along a pipe, the losses will depend on the local conditions along the test section. This approach is therefore not recommendable for supercritical flows, where the fluid properties may have strong gradients along the test section, depending on the specific test conditions.

Combining Equations (1) and (3) gives Equation (22), which well represents the role of enthalpy on heat transfer coefficient determination.

$$\alpha = \frac{\dot{m}\Delta h}{A\Delta T} \tag{22}$$

Expanding Equation (21) further,

$$\frac{u_{q''}}{q''} = \sqrt{\left(\frac{u_{\dot{m}}}{\dot{m}}\right)^2 + \left(\frac{u_{\Delta h}}{\Delta h}\right)^2 + \left(\frac{u_A}{A}\right)^2} \tag{23}$$

For a heat transfer surface equal to $A = \pi D_i L_h$,

$$\frac{u_A}{A} = \sqrt{\frac{\partial A}{\partial L_h} u_L^2 + 2\frac{\partial A}{\partial D_i} u_{D_i}^2} \tag{24}$$

The error in the length determination can be neglected if the pipe is long and the geometry is well known. The individual uncertainty of the diameter, calculated in Section 6.4, is used. Because the calculation of the temperature at the inner wall of the pipe considers the diameter, the contribution of the diameter is multiplied by two in Equation (24).

The enthalpy change term cannot be neglected and is increasingly large when approaching the pseudo-critical point due to a little change in conditions leading to a significant change in heat capacity and, therefore, enthalpy.

$$\left(\frac{u_{\Delta h}}{\Delta h}\right)^2 = \frac{\left[\left(\frac{\partial h}{\partial T}\right)_{P_{out}} u_{T_{out}}\right]^2 + \left[\left(\frac{\partial h}{\partial P}\right)_{T_{out}} u_{P_{out}}\right]^2 + \left[\left(\frac{\partial h}{\partial T}\right)_{P_{in}} u_{T_{in}}\right]^2 + \left[\left(\frac{\partial h}{\partial P}\right)_{T_{in}} u_{P_{in}}\right]^2}{\left(h_{out} - h_{in}\right)^2} \quad (25)$$

where

$$\left(\frac{\partial h}{\partial T}\right)_{P_{in,out}} = C_{p_{in,out}} \quad (26)$$

The derivative of enthalpy with respect to pressure at constant temperature is in general non-zero for real fluids; it can be derived from the first law of thermodynamics and the definition of enthalpy and written as:

$$\left(\frac{\partial h}{\partial P}\right)_T = v - T\left(\frac{\partial v}{\partial T}\right)_P, \quad (27)$$

where v is the specific volume. For an ideal gas, this derivative is neglected because $h = h(T)$ only, but in the supercritical region it becomes significant. In practice, the derivative can be evaluated numerically using REFPROP by changing the pressure while holding the temperature constant:

$$\left(\frac{\partial h}{\partial P}\right)_T \approx \frac{h(T, P + \Delta P) - h(T, P - \Delta P)}{2\,\Delta P}. \quad (28)$$

This approximation with a small pressure step ΔP provides an accurate evaluation of the derivative, which will depend on the fixed temperature value and increase when the pseudo-critical temperature is approached. Figure 7a shows the pressure–enthalpy diagram of carbon dioxide above the critical point. It can be seen that the variation in enthalpy is strongly dependent on temperature at pressures above the critical value. This variation becomes increasingly large at temperatures close to the pseudo-critical temperature at a fixed pressure value. This can be seen for the point at approximately 75.4 bar, where the inflection point at 32 °C corresponds to the pseudo-critical temperature. On the right, Figure 7b shows the enthalpy derivative at the same temperatures, where the effect of both pressure and temperature on the enthalpy of the fluid is visually observed.

These results highlight that the contribution of the enthalpy term to the overall uncertainty is not a fixed quantity, but rather strongly dependent on the local thermodynamic state. In particular, the rapid variation in $h(T, P)$ with both temperature and pressure near the pseudo-critical line (Figure 7) implies that a single, representative value of $u_{\Delta h}/\Delta h$ cannot be defined. Instead, the uncertainty of the heat flux, and consequently of the heat transfer coefficient, must be evaluated at each individual operating condition. This ensures that the propagated uncertainty reflects the actual sensitivity of enthalpy to temperature and pressure at the measurement point, rather than an average or nominal estimate.

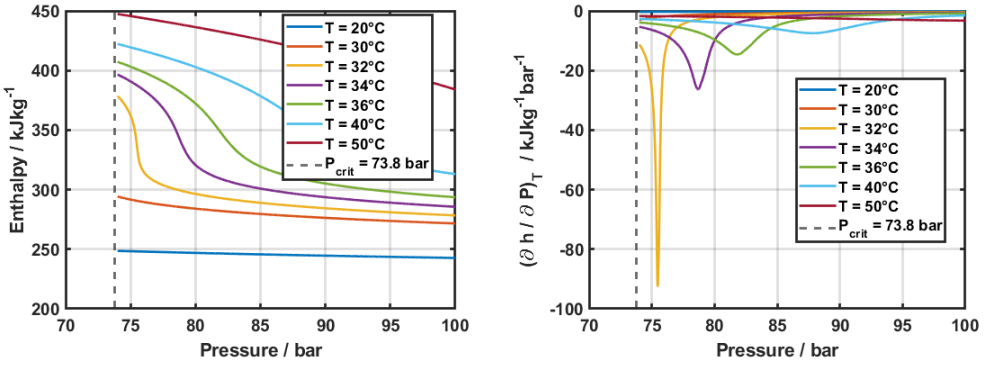

(**a**) (**b**)

Figure 7. Thermodynamic property evaluation in the range 74–90 bar. (**a**) Enthalpy–pressure diagram of carbon dioxide. (**b**) Pressure derivative of enthalpy, $(\partial h/\partial P)_T$.

In practice, the relative uncertainty u_α/α becomes large in a few well-defined situations, consistent with Equation (21) and the expression for $u_{\Delta h}/\Delta h$ given above.

1. When the wall–bulk temperature difference is small, the temperature terms in Equation (21) scale as

$$\sqrt{\left(\frac{u_{T_w}}{\Delta T}\right)^2 + \left(\frac{u_{T_b}}{\Delta T}\right)^2} = \frac{\sqrt{u_{T_w}^2 + u_{T_b}^2}}{\Delta T}, \tag{29}$$

   and therefore grow inversely with ΔT. The effect of different ΔT alone in the uncertainty of the heat transfer coefficient is shown in Figure 6. For this reason, extreme caution must be employed when calibrating the sensors, as their effect expands heavily into the final result.
2. The enthalpy change term can dominate near the pseudo-critical region and the heat capacity $C_p = (\partial h/\partial T)_P$ at either the inlet or the outlet can become very large, so the temperature contributions $(C_{p,out}u_{T_{out}})^2$ and $(C_{p,in}u_{T_{in}})^2$ drive $u_{\Delta h}$. Approximating similar endpoints gives

$$\frac{u_{\Delta h}}{\Delta h} \approx \frac{\sqrt{2}\, C_p\, u_T}{\Delta h},$$

   which shows directly that $u_{\Delta h}/\Delta h$ grows with C_p and shrinks with the enthalpy rise Δh. Because enthalpy is a state function, only the endpoints matter for this propagation: it is sufficient that either the inlet or outlet lies in the high-C_p band for $u_{\Delta h}$ to increase significantly.
   A similar increase in error occurs when the pressure sensitivity $\left(\partial h/\partial P\right)_T$ is large near the pseudo-critical band. In that case, the pressure contributions at the pipe inlet or outlet,

$$\left[\left(\frac{\partial h}{\partial P}\right)_{T_{\text{out}}} u_{P_{\text{out}}}\right]^2 \quad \text{and} \quad \left[\left(\frac{\partial h}{\partial P}\right)_{T_{\text{in}}} u_{P_{\text{in}}}\right]^2, \tag{30}$$

   can rival or exceed the temperature contributions.
   However, in general, both partial derivatives spike when either the inlet or outlet is around the pseudo-critical point, and so they dominate the uncertainty term when that is the case.
3. Even away from the pseudo-critical spike, a small enthalpy rise Δh (light heating, short L_h) increases $u_{\Delta h}/\Delta h$ for a given absolute $u_{\Delta h}$.

Finally, Figure 8 shows the variation in the relative error in the heat transfer coefficient for fixed inlet conditions at three different operational pressures, while varying the outlet

temperature, in a 1 mm pipe with a heated length of 900 mm. Pressure drop data was fixed at 0.8 bar for all three cases and the temperature difference between wall and bulk fluid (ΔT) was assumed to be 3 K.

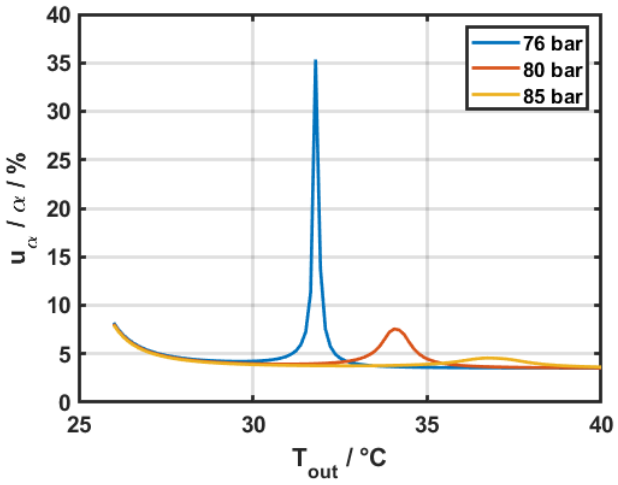

Figure 8. Total uncertainty of the heat transfer coefficient at fixed inlet conditions: $T_{in} = 25$ °C, $P_{in} = 76$ bar, assuming a pressure drop of 0.8 bar and $\Delta T = 3$ K. Individual uncertainties of the process parameters are those calculated in Section 6.

Regarding the effect of roughness, in the turbulent regime relevant to the present experiments ($Re \sim 10^4$–10^5), the dependence of the Darcy friction factor f on the relative roughness ε/D is weak. Using the Swamee–Jain explicit form of the Colebrook relation,

$$f = \frac{0.25}{\left[\log_{10}\left(\frac{\varepsilon/D}{3.7} + \frac{5.74}{Re^{0.9}}\right)\right]^2} \tag{31}$$

the roughness' contribution to the friction factor uncertainty can be estimated from the local sensitivity

$$\frac{u_f}{f} \approx \left|\frac{\partial \ln f}{\partial \ln \varepsilon}\right| \frac{u_\varepsilon}{\varepsilon} \tag{32}$$

For $D \simeq 1$ mm, $\varepsilon = 1.15 \pm 0.05$ µm (thus $\varepsilon/D \simeq 1.1 \times 10^{-3}$ and $u_\varepsilon/\varepsilon \simeq 4.3\%$) and a representative Reynolds number of $Re = 10^5$, this yields $u_f/f \simeq 0.7\%$.

The segment-wise frictional pressure drop is computed using Darcy–Weisbach, $\Delta P = f\,(L/D)\,(\rho v^2/2)$; hence, $\Delta P \propto f$ and therefore

$$\frac{u_{\Delta P,\varepsilon}}{\Delta P} \approx \frac{u_f}{f} \simeq 0.7\% \tag{33}$$

Assuming a $\Delta P \sim 1$ bar over the heated length, this gives $u_{\Delta P,\varepsilon} \lesssim 0.007$ bar, which is small compared with the absolute pressure uncertainty ($u_P \approx 0.2$ bar).

The roughness-induced pressure-drop uncertainty contributes to the enthalpy-rise uncertainty through $(\partial h/\partial P)_T\, u_{\Delta P,\varepsilon}$, which is negligible compared with the dominant temperature and mass flow contributions. Consequently, the contribution of roughness uncertainty to u_α/α is neglected.

9. Validation

Validation of the test rig under conditions where established correlations are applicable is a necessary step before extracting data in the supercritical regime. For this purpose, measurements were carried out at sub-critical liquid conditions, where the thermophysical

properties do not change or vary only moderately along the pipe. Under these conditions, both the pressure drop and the heat transfer coefficient can be directly compared with well-established correlations.

Figure 9 shows the measured wall-to-bulk temperature difference along the heated section, together with the resulting experimental heat transfer coefficient profile. For comparison, heat transfer coefficients were evaluated using the Gnielinski correlation. The data reduction procedure is that specified in Section 7.

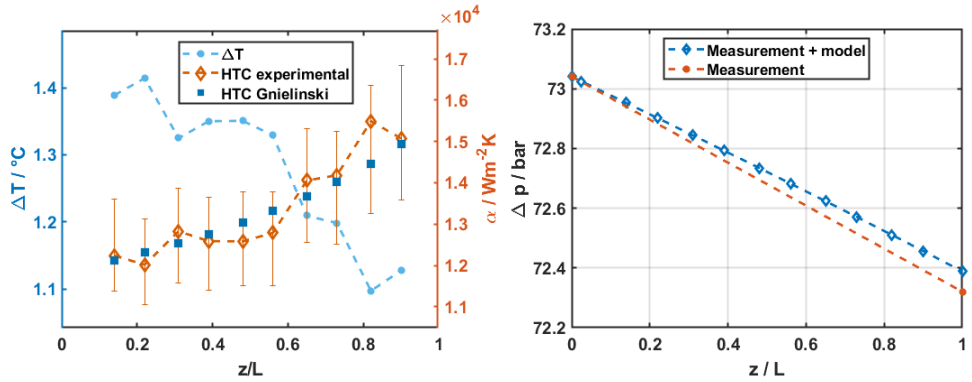

(**a**) (**b**)

Figure 9. Results of the sub-critical subcooled test validation with carbon dioxide at $P_{in} = 73$ bar, $T_{in} = 19.9$ °C, $\dot{Q} = 50$ W, $\dot{m} = 1.8$ g/s, $D_i = 1.04$ mm, $L_h = 0.9$ m, $L = 1$ m. (**a**) Temperature difference and heat transfer coefficient along the pipe axial length. (**b**) Pressure profile along the axial length.

Uncertainty bars are included, representing the propagated uncertainty of the heat transfer coefficient as described in Section 8.

Overall, the measured heat transfer coefficients are in very good agreement with the Gnielinski correlation. Additionally, the calculated pressure drops are well captured by the Darcy–Weisbach/McAdams approach, with errors below 1%. This confirms that the test rig is operating reliably and provides confidence in its use for subsequent measurements under supercritical conditions.

In this figure, it is observed that the uncertainty bars become larger at smaller ΔT values, which is in line with the trends deducted in this manuscript.

To assess repeatability, selected operating points were repeated on different days, with the facility fully shut down and restarted between runs. The relative difference in the local heat transfer coefficient between repeated measurements was typically below 5% in the liquid-like region (away from the pseudo-critical regime), with most data points showing deviations of only a few percent, demonstrating good experimental stability. Under such conditions, the relative difference in pressure drop measurements remained below 1%.

10. Conclusions

A modular test rig to study heat transfer with supercritical carbon dioxide has been developed and validated. All necessary technical information has been included in this manuscript. In addition, the individual calibration of wall and in-fluid temperature sensors has been presented in detail and the importance of accurate temperature measurements for heat transfer coefficient derivation has been demonstrated. To support this, an in-depth calculation of the uncertainty relative to the experimental local heat transfer coefficient has been carried out. This analysis has shown that the temperature uncertainty dominates when the wall–bulk temperature difference is small, while the enthalpy-change term

becomes critical near the pseudo-critical region due to its strong sensitivity with respect to temperature and pressure.

Certain practical considerations can be identified to maintain a controlled relative uncertainty in the heat transfer coefficient. A primary factor is the thermodynamic proximity of the inlet and outlet states to the pseudo-critical region. When either endpoint lies close to the pseudo-critical temperature at a given pressure—particularly at pressures near the critical value—the strong gradients in thermophysical properties significantly increase the propagated uncertainty of the enthalpy rise. Consequently, operating points in this region inherently carry higher relative uncertainty and require careful thermodynamic evaluation. Furthermore, sufficient thermal input is required to ensure a measurable enthalpy rise. For a given absolute measurement accuracy, a small enthalpy increase leads to a larger relative uncertainty in Δh, directly affecting the derived heat transfer coefficient.

In addition, small wall–bulk temperature differences amplify the contribution of temperature measurement uncertainty, as demonstrated in the preceding derivation. These effects do not prevent operation in such regimes, but rather highlight that low driving temperature differences demand proportionally higher measurement accuracy and careful uncertainty propagation.

Indeed, the reliability of the heat transfer coefficient determination depends critically on the individual calibration and characterization of all temperature and pressure sensors involved. Detailed and transparent reporting of calibration procedures is therefore essential for meaningful comparison of results across different experimental facilities.

Finally, experiments with sub-critical subcooled liquid flow were carried out to validate the experimental measurements with respect to analytical calculations. The comparison with known correlations and models has shown good agreement with the theory, showing the robustness of the rig and its acquisition system.

The rig will continue operation and studies characterizing the heat transfer coefficient and pressure drop at supercritical conditions are expected soon.

Supplementary Materials: The following supporting information can be downloaded at: https://www.mdpi.com/article/10.3390/hardware4020007/s1.

Name	Type	Description
charts	Images (.zip)	Miscellaneous images used for the development of the p-h diagram in the front panel
config	Configuration files (.zip)	Constants related to the positions of sensors and their calibration constants specific to the current test section installed
controls	Control files (.zip)	Structure of certain variables contained in the main LabVIEW code
pictures	Pictures (.zip)	Pictures of the test setup
src\labview	LabVIEW code (.zip)	Main and subvis of CO_2-SASS
sco2	LabVIEW project (.zip)	LabVIEW project file

Author Contributions: Methodology, C.P.-M., P.P. and S.G.; Software, C.P.-M.; Validation, C.P.-M.; Formal analysis, C.P.-M.; Investigation, C.P.-M.; Data curation, C.P.-M.; Writing—original draft, C.P.-M.; Writing—review & editing, C.P.-M., P.P. and S.G.; Visualization, C.P.-M.; Supervision, P.P. and S.G.; Project administration, P.P.; Funding acquisition, P.P. All authors have read and agreed to the published version of the manuscript.

Funding: This project received funding from the European Union's Horizon 2020 Research and Innovation programme under Grant Agreement No. 101004761. This work was supported by the Wolfgang Gentner Programme of the German Federal Ministry of Education and Research (BMBF).

Data Availability Statement: The original contributions presented in this study are included in the article and Supplementary Material. Further inquiries can be directed to the corresponding author.

Acknowledgments: The electrical cabinet of this test rig was built by Andrzej Baran (CERN). Further work performed by Jarl Pettersen (CERN). The data acquisition software was designed with the help of Elena Galetti and the BE-CEM-MTA section at CERN. During the preparation of this manuscript/study, the authors used ChatGPT 4.0 for the purposes of assistance in the correct structure and rephrasing of some statements in the text. The authors have reviewed and edited the output and take full responsibility for the content of this publication.

Conflicts of Interest: The authors declare no conflicts of interest.

Abbreviations

The following abbreviations are used in this manuscript:

A	Heat transfer surface area [m^2]
c_p	Specific heat at constant pressure [$J\,kg^{-1}\,K^{-1}$]
CF	Correction factor for conduction [-]
CS	Cross-sectional area of flow [m^2]
D_i	Inner diameter of tube [m]
D_o	Outer diameter of tube [m]
f	Darcy friction factor [–]
h	Specific enthalpy [$J\,kg^{-1}$]
L	Total tube length [m]
L_h	Heated length of tube [m]
$\dot{m}$	Mass flow rate [$kg\,s^{-1}$]
Nu	Nusselt number [–]
p	Pressure [bar]
P_{in}	Inlet pressure [bar]
P_{out}	Outlet pressure [bar]
Pr	Prandtl number [–]
q	Heat input [W]
q''	Heat flux [$W\,m^{-2}$]
$\dot{Q}$	Total heat transfer rate [W]
Re	Reynolds number [–]
T	Temperature [K or °C]
T_b	Bulk fluid temperature [K or °C]
T_{in}	Inlet temperature [K or °C]
T_{out}	Outlet temperature [K or °C]
T_w	Wall temperature [K or °C]
Δh	Enthalpy difference [$J\,kg^{-1}$]
Δp	Pressure drop [bar]
ΔT	Wall-to-bulk temperature difference [K]
ΔT_w	Wall temperature difference (outer–inner wall) [K]
u	Standard uncertainty [various units]
u_x/x	Relative uncertainty of quantity x [%]
α	Heat transfer coefficient [$W\,m^{-2}\,K^{-1}$]
λ	Thermal conductivity [$W\,m^{-1}\,K^{-1}$]
μ	Dynamic viscosity [Pa s]
ψ	Geometrical relationship between outer and inner diameter [-]
ρ	Density [$kg\,m^{-3}$]

z	Axial coordinate along the tube [m]
z/L	Dimensionless axial coordinate [–]

Appendix A. Thermocouple Calibration

Thermocouples measure voltage difference between a hot and a cold junction. This means that when the voltage difference is the output of the DAQ, this corresponds to:

$$\Delta V = V_{hot} - V_{cold} \tag{A1}$$

which, by the working principle of a thermocouple, corresponds to:

$$\Delta T = T_{hot} - T_{cold} \tag{A2}$$

To calibrate each thermocouple individually from the temperature at the cold junction, V_{hot} must be calculated.

The cold junction temperature is obtained from the thermistor voltage using a voltage divider and the Steinhart–Hart equation:

$$R_t = R_s \cdot \frac{V_{\text{meas}}}{V_{\text{ref}} - V_{\text{meas}}} \tag{A3}$$

$$T_{\text{CJC}} = \left[a + b \cdot \ln(R_t) + c \cdot (\ln(R_t))^2\right]^{-1} - 273.15 \tag{A4}$$

$$\begin{aligned} a &= 1.265361 \times 10^{-3} \\ b &= 2.343159 \times 10^{-4} \\ c &= 1.018703 \times 10^{-7} \end{aligned} \tag{A5}$$

The ITS-90 defines two equations to obtain temperature from voltage and vice versa:

$$E(T) = \sum_{i=0}^{9} c_i T^i + \alpha_0 \cdot \exp\left[\alpha_1 \cdot (T - 126.9686)^2\right] \tag{A6}$$

$$\begin{aligned} c_0 &= -1.7600413686 \times 10^{1} \\ c_1 &= 3.8921204975 \times 10^{1} \\ c_2 &= 1.8558770032 \times 10^{-2} \\ c_3 &= -9.9457592874 \times 10^{-5} \\ c_4 &= 3.1840945719 \times 10^{-7} \\ c_5 &= -5.6072844889 \times 10^{-10} \\ c_6 &= 5.6075059059 \times 10^{-13} \\ c_7 &= -3.2020720003 \times 10^{-16} \\ c_8 &= 9.7151147152 \times 10^{-20} \\ c_9 &= -1.2104721275 \times 10^{-23} \end{aligned} \tag{A7}$$

$$\begin{aligned} \alpha_0 &= 1.185976 \times 10^{2} \\ \alpha_1 &= -1.183432 \times 10^{-4} \end{aligned} \tag{A8}$$

To convert a measured voltage E (in millivolts) to temperature $T(E)$ in degrees Celsius, the inverse polynomial equation is used (valid for $0 \leq E \leq 54.886$ mV):

$$T(E) = \sum_{i=0}^{9} d_i E^i \tag{A9}$$

$$
\begin{aligned}
d_0 &= 0.000000000000 \\
d_1 &= 2.508355 \times 10^{1} \\
d_2 &= 7.860106 \times 10^{-2} \\
d_3 &= -2.503131 \times 10^{-1} \\
d_4 &= 8.315270 \times 10^{-2} \\
d_5 &= -1.228034 \times 10^{-2} \\
d_6 &= 9.804036 \times 10^{-4} \\
d_7 &= -4.413030 \times 10^{-5} \\
d_8 &= 1.057734 \times 10^{-6} \\
d_9 &= -1.052755 \times 10^{-8}
\end{aligned}
\tag{A10}
$$

The workflow of the calibration procedure is shown in Figure A1. The data from the top is acquired at the same time in the conditions specified above. The rhomboids represent conversions or processes applied to the data. The goal of this process is to:

- Obtain individual equations to describe the thermocouple behavior in the range of interest.
- Characterize the cold junction error and evaluate its feasibility for wall temperature measurements.
- Calculate the derived uncertainty of the wall temperature measurement.

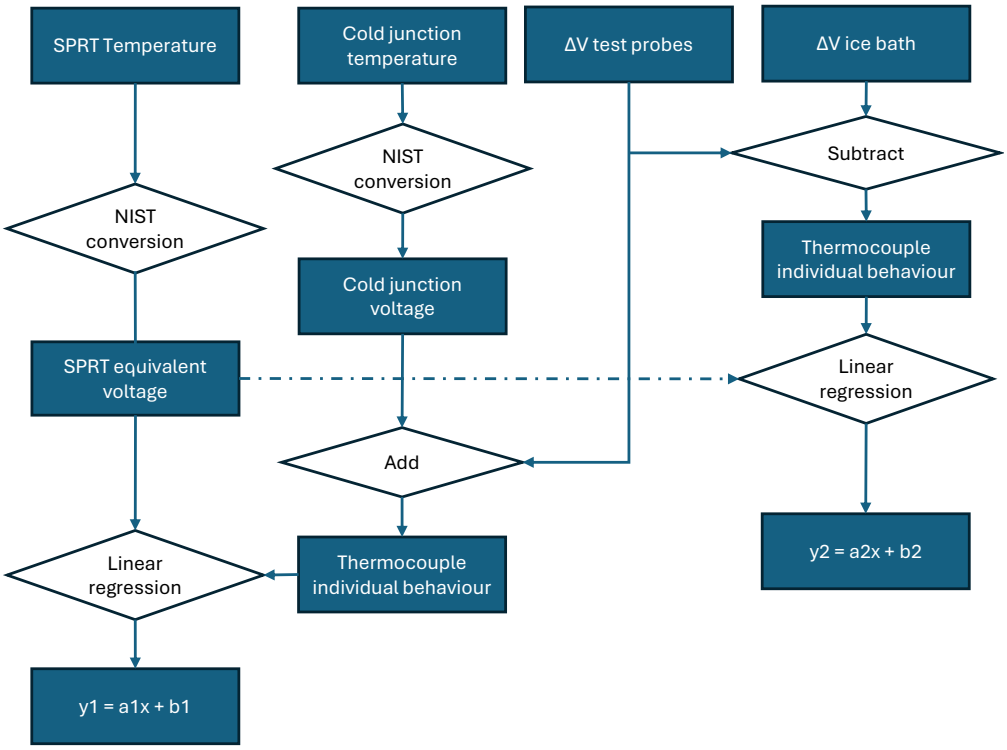

Figure A1. Schematic of the thermocouple calibration and correction process. The SPRT reference temperature is converted to voltage using the NIST ITS-90 equation. Each thermocouple reading is compensated for cold junction effects and corrected for individual behavior using a linear calibration.

The leftmost fit will be the individuated thermocouple result using the electronic cold junction and the rightmost will correspond to the result using an ice bath as a reference. The same applies to Figure A2, where it is observed that the systematic behavior of the thermocouple in question is quite linear for the operating range; however, the intercept of the leftmost fit shows that the systematic correction needed to compensate for the

uncertainty of the cold junction temperature is 0.0156 mV. Considering that the sensitivity of a type K thermocouple is 41 µV/K, this corresponds to a systematic correction of 0.38 °C. This agrees with the maximum accuracy value reported by NI on NI9214.

On the other hand, the rightmost fit shows a systematic correction of 0.0024 µV when the ice bath is used, translating to a systematic temperature drift of 0.05 °C. This aligns better with the goal of staying below a 0.2 K wall temperature error. The maximum error (RMSE) in both cases was 0.021 °C. Physically speaking, the combination of the two offsets results in systematic bias in the cold junction, which can be applied to each thermocouple individually to account for the cold junction error.

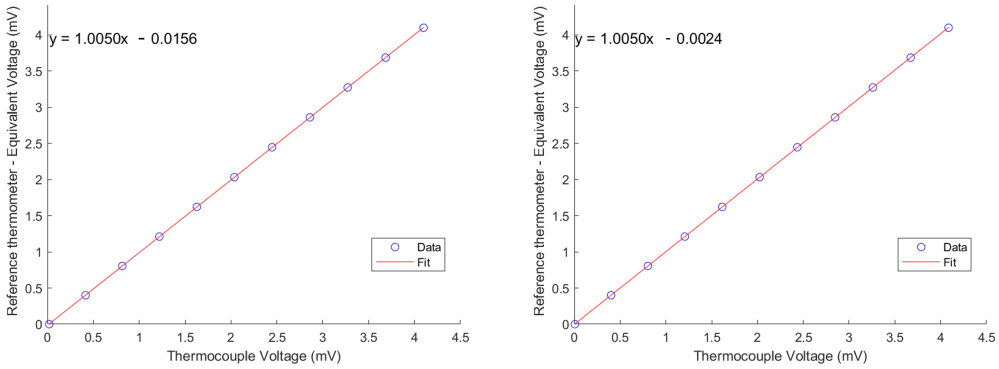

(**a**) Electronic cold junction measurement. (**b**) Ice measurement.

Figure A2. Voltage calibration for one example probe against ITS-90 equivalent reference voltage.

The two calibration equations obtained for the thermocouple are:

$$V_{\text{ref, CJC}} = 1.0050 \cdot V_{\text{meas}} - 0.0156 \text{ mV} \tag{A11}$$

$$V_{\text{ref, ice}} = 1.0050 \cdot V_{\text{meas}} - 0.0024 \text{ mV} \tag{A12}$$

Subtracting Equation (7) from Equation (8) yields the voltage difference between the two methods:

$$\Delta V = V_{\text{ref, ice}} - V_{\text{ref, CJC}} = 0.0132 \text{ mV} \tag{A13}$$

The physical meaning of this subtraction corresponds to the error of the cold junction. This implies that the cold junction measurement introduces a systematic offset of 0.0132 mV. Given the sensitivity of type K thermocouples, this voltage offset translates to a temperature correction of:

$$\Delta T = \frac{0.0132 \text{ mV}}{0.041 \text{ mV}/^{\circ}\text{C}} \approx 0.32 \,^{\circ}\text{C} \tag{A14}$$

This means that, even if the accuracy of the thermocouple calibration is low, the electronic cold junction introduces a significant error into the wall temperature measurement equal to:

$$V_{\text{corrected}} = V_{\text{meas}} + 0.0132 \text{ mV} \tag{A15}$$

Or, equivalently, the corrected temperature could be obtained as:

$$T_{\text{corrected}} = T(V_{\text{meas}} + 0.0132) \tag{A16}$$

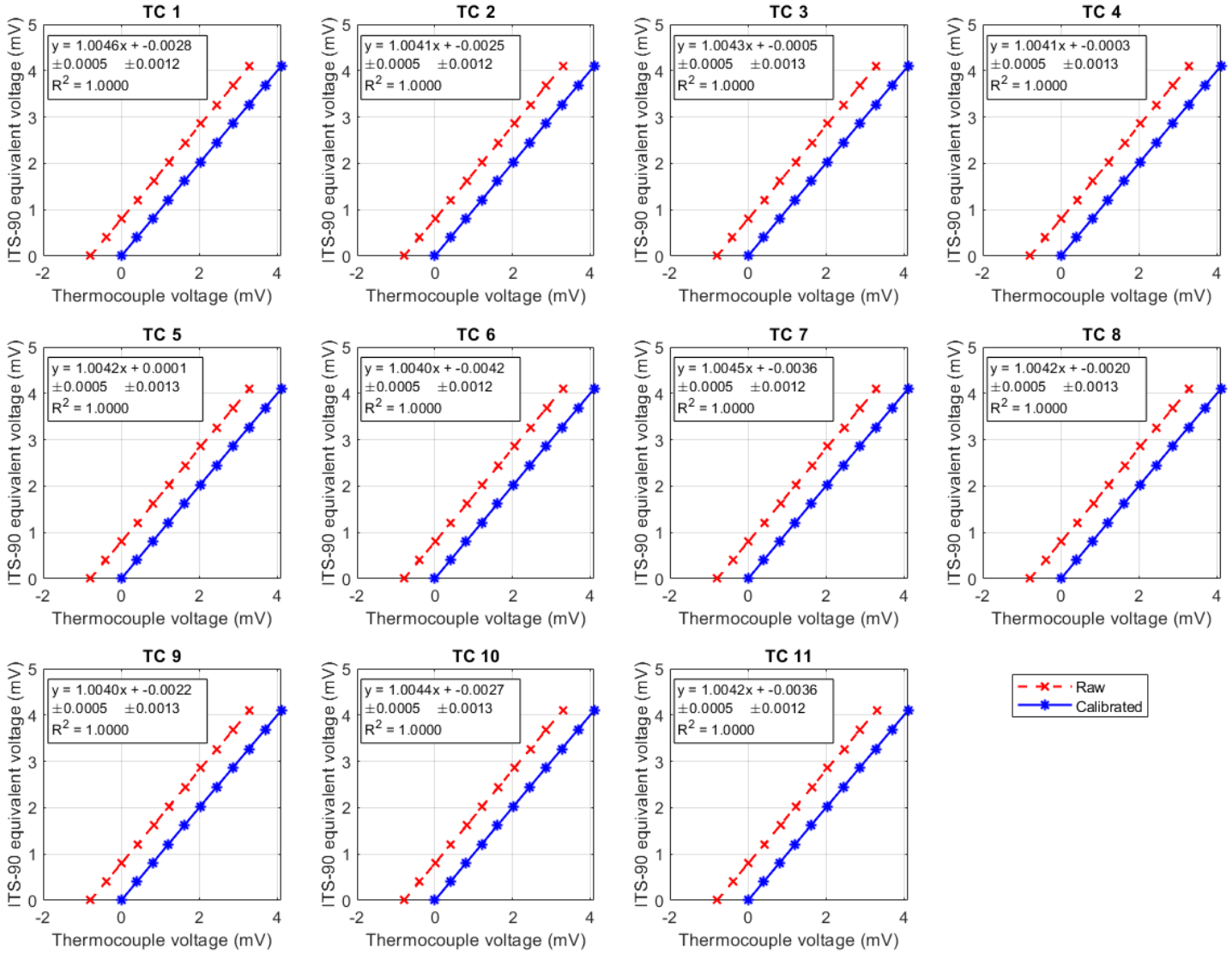

Figure A3. Calibration fits for wall thermocouples (TC1–TC11). Red: raw measurements; blue: calibrated values. Linear fits with slope and intercept ($\pm 1\sigma$) are shown in each panel, as well as R^2.

Appendix B. PT-100

The guidelines of the ITS-90 are based on comparing the resistance ratio of each individual probe to that of a precise reference thermometer. With the reference thermometer reading $T_{\mathrm{ref,C}}$ (in °C), the reference resistance ratio can be calculated.

$$T_{\mathrm{ref,K}} = T_{\mathrm{ref,C}} + 273.15, \qquad \theta = \frac{T_{\mathrm{ref,K}} - 754.15}{481} \tag{A17}$$

$$W_{\mathrm{ref}} = \sum_{n=0}^{9} C_n \, \theta^n \tag{A18}$$

The forward coefficients are:

$$\mathbf{C} = \begin{bmatrix} 2.78157254 \\ 1.64650916 \\ -0.13714390 \\ -0.00649767 \\ -0.00234444 \\ 0.00511868 \\ 0.00187982 \\ -0.00204472 \\ -0.00046122 \\ 0.00045724 \end{bmatrix} \tag{A19}$$

Given the probe's TPW resistance R_{TPW} and the measured resistance R, the ratio and deviation function from the reference can be calculated.

$$W = \frac{R}{R_{\mathrm{TPW}}}, \qquad \Delta W = W - W_{\mathrm{ref}} \tag{A20}$$

A least-squares fit is performed to obtain the parameter a so that:

$$\Delta W = a \, (W - 1) \tag{A21}$$

Finally, the RMSE can be calculated using:

$$\mathrm{RMSE} = \sqrt{\frac{1}{N} \sum (\Delta W - \widehat{\Delta W})^2} \tag{A22}$$

Finally, the corresponding temperature is calculated with Equation (A24).

$$x = \frac{W_r - 2.64}{1.64} \tag{A23}$$

$$T_{\mathrm{cal}} = \sum_{n=0}^{9} D_n \, x^n \quad (^{\circ}\mathrm{C}) \tag{A24}$$

for which the coefficients are:

$$\mathbf{D} = \begin{bmatrix} 439.932854 \\ 472.418020 \\ 37.684494 \\ 7.472018 \\ 2.920828 \\ 0.005184 \\ -0.963864 \\ -0.188732 \\ 0.191203 \\ 0.049025 \end{bmatrix} \tag{A25}$$

Figure A4 shows the least-squares fit as per the ITS-90 for the range 0–156.6 °C.

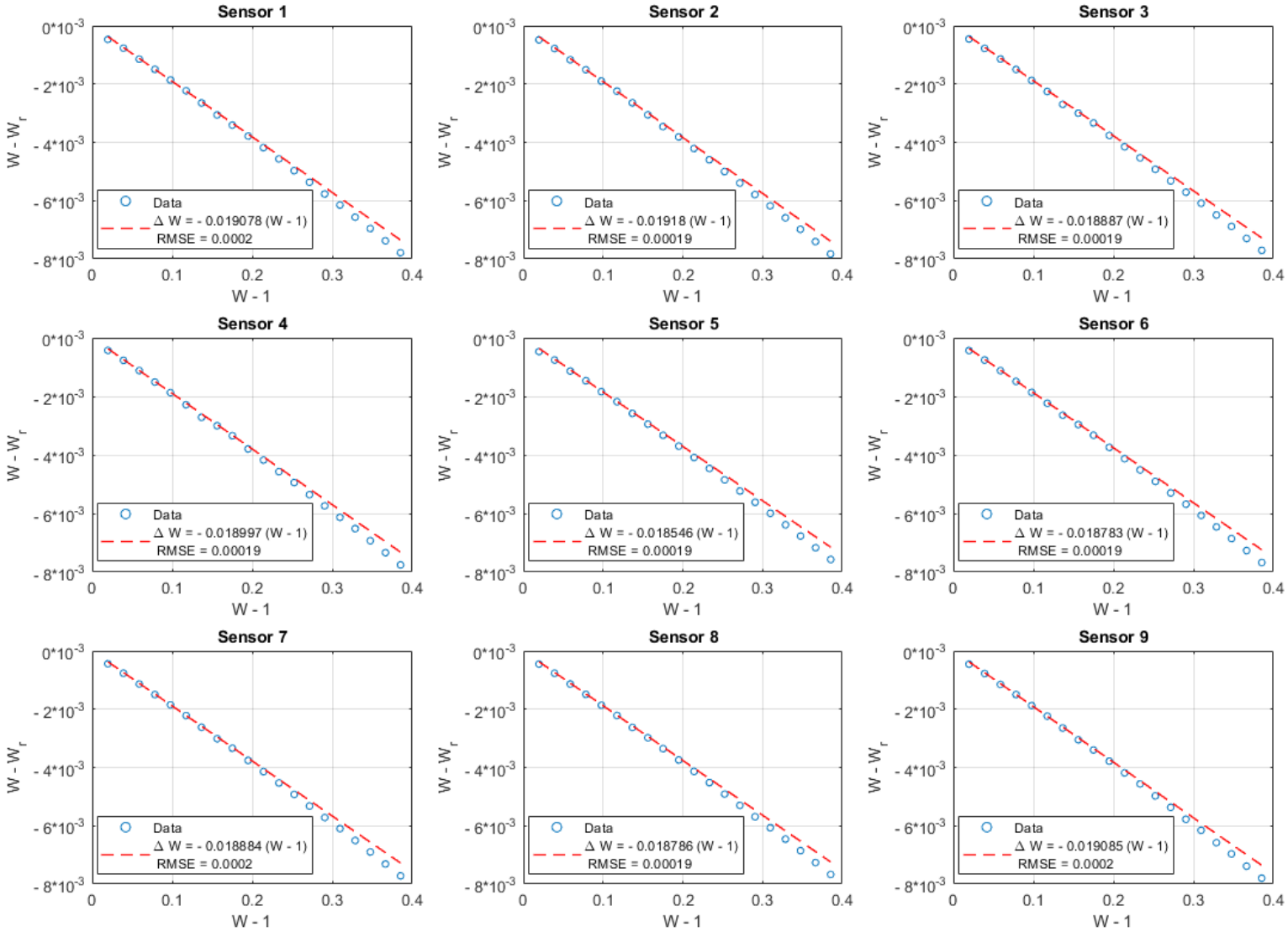

Figure A4. Calibration of PT100 sensors using the resistance ratio method. Plotted is ΔW versus $W - 1$ for all nine sensors, with linear fits shown in red. The fitted slopes and RMSE values indicate excellent agreement and reproducibility across sensors.

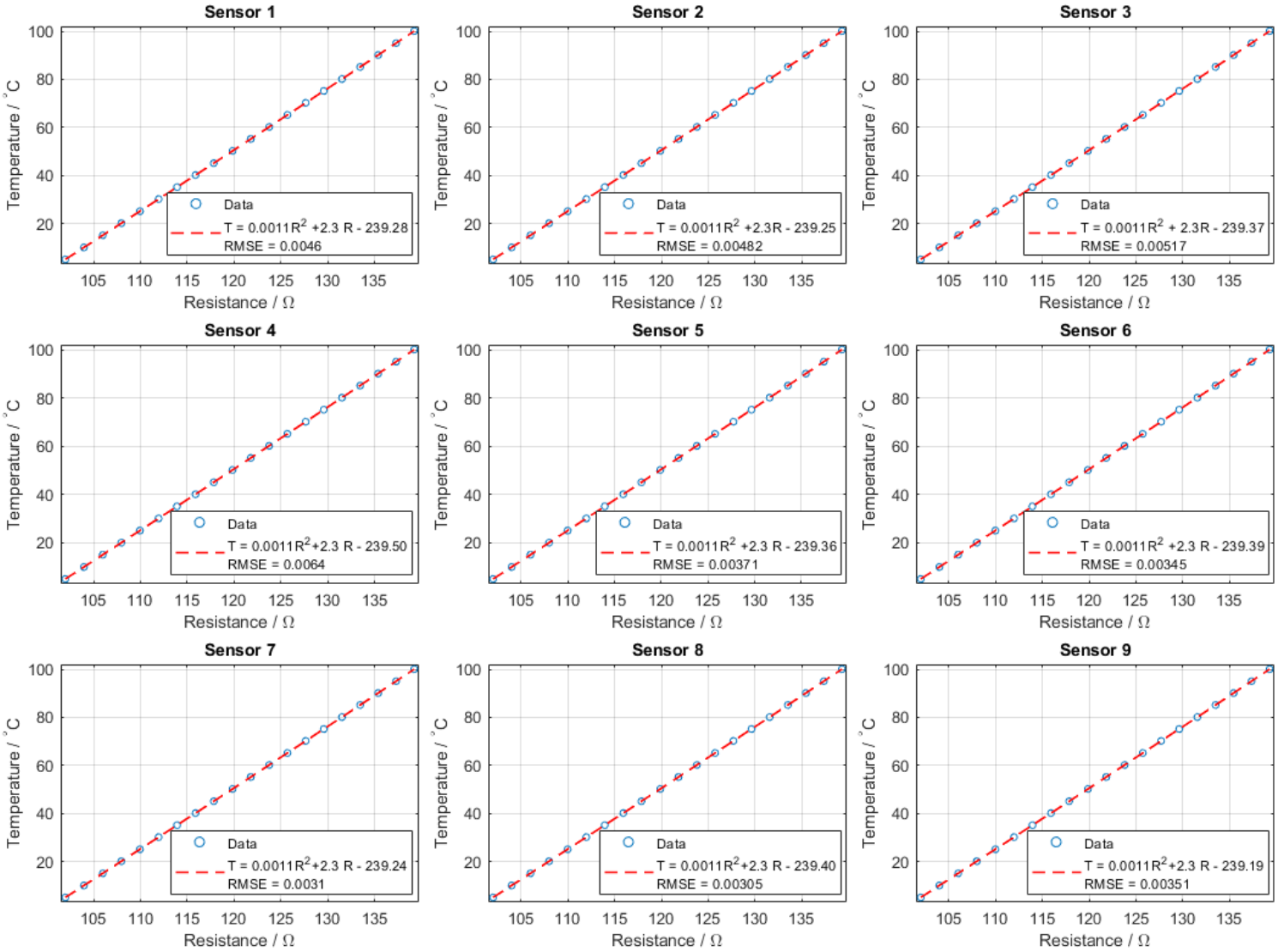

Figure A5. Operational calibration of PT100 sensors. The plots show temperature as a function of resistance for all nine sensors, with polynomial fits (red dashed) compared against experimental data (blue). RMSE values remain below 0.01 °C, confirming the sensors' accuracy during operation.

References

1. Kwon, J.S.; Son, S.; Heo, J.Y.; Lee, J.I. Compact Heat Exchangers for Supercritical CO_2 Power Cycle Application. *Energy Convers. Manag.* **2020**, *209*, 112666. [CrossRef]
2. Stottlemyre, W.; Nordlund, A.; Gess, J.; Ramakrishnan, B.; Alissa, H. Experimental Evaluation of Supercritical Carbon Dioxide as a Viable Coolant for Electronics Thermal Management. Available online: https://www.electronics-cooling.com/2023/12/experimental-evaluation-of-supercritical-carbon-dioxide-as-a-viable-coolant-for-electronics-thermal-management/ (accessed on 2 July 2025).
3. Fronk, B.M.; Rattner, A.S. High-Flux Thermal Management with Supercritical Fluids. *J. Heat Transf.* **2016**, *138*, 124501. [CrossRef]
4. Guo, P.; Liu, S.; Yan, J.; Wang, J.; Zhang, Q. Experimental Study on Heat Transfer of Supercritical CO_2 Flowing in a Mini Tube under Heating Conditions. *Int. J. Heat Mass Transf.* **2020**, *153*, 119623. [CrossRef]
5. Lei, X.; Peng, R.; Guo, Z.; Li, H.; Ali, K.; Zhou, X. Experimental Comparison of the Heat Transfer of Carbon Dioxide under Subcritical and Supercritical Pressures. *Int. J. Heat Mass Transf.* **2020**, *152*, 119562. [CrossRef]
6. Wang, X.; Yang, L.; Xu, B.; Chen, Z. Experimental Study on Heat Transfer and Flow Characteristics of Supercritical CO_2: In-depth Analysis of Three Heat Transfer Coefficients. *Int. J. Heat Mass Transf.* **2025**, *241*, 126748. [CrossRef]
7. Liao, S.; Zhao, T. An Experimental Investigation of Convection Heat Transfer to Supercritical Carbon Dioxide in Miniature Tubes. *Int. J. Heat Mass Transf.* **2002**, *45*, 5025–5034. [CrossRef]
8. Wang, L.; Pan, Y.C.; Der Lee, J.; Wang, Y.; Fu, B.R.; Pan, C. Experimental Investigation in the Local Heat Transfer of Supercritical Carbon Dioxide in the Uniformly Heated Horizontal Miniature Tubes. *Int. J. Heat Mass Transf.* **2020**, *159*, 120136. [CrossRef]
9. Cabeza, L.F.; de Gracia, A.; Fernández, A.I.; Farid, M.M. Supercritical CO_2 as Heat Transfer Fluid: A Review. *Appl. Therm. Eng.* **2017**, *125*, 799–810. [CrossRef]
10. Ferrand, T.; Oettig, J.; Schäfer, L.; Gschnaidtner, T.; Naja, M.O.; Wieland, C.; Spliethoff, H. A Limitation to Determine Heat Transfer of Water at Supercritical Pressure: The Repeatability Issue. *Appl. Therm. Eng.* **2023**, *219*, 119357. [CrossRef]
11. Huber, M.; Harvey, A.; Lemmon, E.; Hardin, G.; Bell, I.; McLinden, M. NIST Reference Fluid Thermodynamic and Transport Properties Database (REFPROP) Version 9.1—SRD 23, 2018. Available online: https://www.nist.gov/srd/refprop (accessed on 1 October 2025). [CrossRef]
12. National Institute of Standards and Technology. *Ice Point Calibration*; National Institute of Standards and Technology: Gaithersburg, MD, USA, 2014. Available online: https://www.youtube.com/watch?v=KYOJayWqB3g (accessed on 15 March 2026).
13. Preston-Thomas, H. The International Temperature Scale of 1990 (ITS-90). *Metrologia* **1990**, *27*, 107. Available online: https://iopscience.iop.org/article/10.1088/0026-1394/27/2/010 (accessed on 1 October 2025). [CrossRef]
14. Buongiorno, J. Methodologies to Select Friction Factor and Convective Heat Transfer Correlations for Single-Phase Fluids. 2014. Available online: https://tinyurl.com/shortened-link-to-mit-edu (accessed on 15 March 2026).
15. Wang, Z.; Sun, B.; Wang, J.; Hou, L. Experimental Study on the Friction Coefficient of Supercritical Carbon Dioxide in Pipes. *Int. J. Greenh. Gas Control* **2014**, *25*, 151–161. [CrossRef]

Disclaimer/Publisher's Note: The statements, opinions and data contained in all publications are solely those of the individual author(s) and contributor(s) and not of MDPI and/or the editor(s). MDPI and/or the editor(s) disclaim responsibility for any injury to people or property resulting from any ideas, methods, instructions or products referred to in the content.